

# Near edge X-ray absorption fine structure measurements (XANES) and extended x-ray absorption fine structure measurements (EXAFS) of the valence state and coordination of antimony in doped nanocrystalline SnO<sub>2</sub>

J. Rockenberger<sup>a)</sup> and U. zum Felde

*Institut für Physikalische Chemie, Universität Hamburg, Bundesstrasse 45, D-20146 Hamburg, Germany*

M. Tischer and L. Tröger

*Hamburger Synchrotronstrahlungslabor HASYLAB, Deutsches Elektronen-Synchrotron DESY, Notkestrasse 85, D-22603 Hamburg, Germany*

M. Haase<sup>b)</sup> and H. Weller

*Institut für Physikalische Chemie, Universität Hamburg, Bundesstrasse 45, D-20146 Hamburg, Germany*

(Received 14 June 1999; accepted 1 December 1999)

Colloids of nanocrystalline tin dioxide containing 9.1 at. % and 16.7 at. % antimony have been prepared by the coprecipitation method. High-resolution transmission electron microscopy (TEM) images show crystalline particles in the 2–6 nm size regime. X-ray powder diffraction patterns of nanocrystalline powders obtained by drying the colloids and heating to 100 °C indicate the same rutile lattice structure known from bulk SnO<sub>2</sub>. On heating to 500 °C in air, the nanocrystalline powder shows a slight increase in particle size but especially a change in color from yellowish to bluish which is accompanied by the development of *n*-type conductivity. The coordination of antimony in the SnO<sub>2</sub> nanocrystallites has been investigated by extended x-ray absorption fine structure measurements (EXAFS) at the Sb *K*-edge at 5 K while its valence state was determined by near edge x-ray absorption fine structure measurements (XANES) at the Sb *L*<sub>1</sub> edge. The Sb higher neighbor shell distances in the doped material differ from the corresponding distances in Sb<sub>2</sub>O<sub>3</sub> or Sb<sub>2</sub>O<sub>5</sub> but are identical to those in tin dioxide, indicating that antimony is almost completely incorporated into the tin dioxide lattice despite the high doping level. XANES measurements reveal that a large fraction of Sb<sup>III</sup> employed during the synthesis is already oxidized to Sb<sup>V</sup> at low temperatures. On the basis of these observations, a two-step model for the formation of *n*-conductive Sb-doped SnO<sub>2</sub> nanocrystals is given and quantitatively discussed with respect to the data. © 2000 American Institute of Physics. [S0021-9606(00)70208-X]

## I. INTRODUCTION

The physical and chemical properties of colloidal nanocrystals have been of widespread interest and have been described in several reports and review articles.<sup>1–9</sup> While a large variety of colloids of nanocrystalline materials has been prepared successfully by wet-chemical synthesis, only a comparatively small number of reports has been published on doped nanoparticles prepared by this method.<sup>10–19</sup>

One of the nanocrystalline systems that can easily be prepared as a colloid is tin dioxide.<sup>20</sup> Bulk stoichiometric tin dioxide<sup>21,22</sup> is an insulator with a band gap of about 3.8 eV.<sup>23</sup> High *n*-type conductivity is observed in tin dioxide if it is either oxygen deficient or doped with atoms such as fluorine or antimony.<sup>24</sup> At doping levels of about 2% to 7% antimony, a degenerate semiconductor is formed, displaying metallic properties.<sup>25–27</sup> If the doping level is not too high, conductive films of SnO<sub>2</sub>:Sb deposited on glass are transparent for visible light and have been of interest<sup>28</sup> for their potential

use in photovoltaic and optoelectronic devices, flat panel displays, etc. Due to the presence of free charge carriers, the conductive SnO<sub>2</sub>:Sb films exhibit a high absorption coefficient in the infrared (IR) region. As a consequence, these films are highly reflective for IR radiation, making them usable for heat shields.<sup>29,30</sup> The IR spectrum of these films can be reasonably well described by applying simple Drude theory for a free electron gas.<sup>31,32</sup> Within this theory, the spectral onset of the IR reflection is described by the plasma frequency, which depends on the concentration and the mean free path of the carriers. The free carrier concentration in the material can easily be varied by changing the concentration of dopant atoms. At low doping levels, antimony is incorporated in SnO<sub>2</sub> almost exclusively as Sb<sup>V</sup>.<sup>33</sup> If the concentration of antimony is increased above ~4%–7%, however, an increasing amount of antimony in the oxidation state 3+ is incorporated into the lattice. The latter is accompanied by a decrease in conductivity.<sup>34</sup>

Nevertheless, tin dioxide containing a high amount of antimony is of technological importance, too, as it presents a good catalyst for the selective oxidation of olefins.<sup>35,36</sup> The catalysts as well as the conductive films consist of dioxide particles in the nanometer size regime.

<sup>a)</sup>Present address: Department of Chemistry, University of California, Berkeley, Box 101, Berkeley, California.

<sup>b)</sup>Author to whom correspondence should be addressed. Electronic mail: haase@chemie.uni-hamburg.de

Since the valence state of the antimony dopant as well as the local geometry of the antimony sites are considered to be of crucial importance for the catalytic and electronic properties of the mixed oxide, tin antimony oxides have been investigated by several methods including x-ray diffraction,<sup>37</sup> neutron diffraction,<sup>38</sup> ultraviolet<sup>39</sup> and x-ray photoelectron spectroscopy,<sup>39–42</sup> and Mössbauer spectroscopy.<sup>33</sup> Despite these efforts, the nature of the antimony sites in highly doped nanocrystalline SnO<sub>2</sub> is still not well understood.

In an attempt to directly probe the local atomic environment and the valence state of antimony in doped tin dioxide, we performed an EXAFS and XANES study on doped nanocrystalline tin dioxide powders prepared from colloidal solutions. Tin dioxide nanocrystals with two different antimony contents (9.1 and 16.7 at. %), treated at different temperatures (100 °C and 500 °C) have been investigated. The structural results obtained are then compared with the electrical properties of thin films prepared by spin-coating glass substrates with the colloidal solutions.

EXAFS studies of the local environment of tin in pure tin dioxide<sup>43,44</sup> as well as of europium,<sup>45</sup> copper, and iron<sup>46</sup> in doped SnO<sub>2</sub> have already been reported in the literature.

## II. EXPERIMENTAL SECTION

### A. Preparation

Colloidal tin antimony oxide was prepared by the coprecipitation method using a procedure similar to those given in the literature.<sup>47–49</sup>

In brief, an appropriate amount of SbCl<sub>3</sub> was dissolved in fuming HCl (37 wt %) and the clear solution was dropped into a solution of 85 mmol SnCl<sub>4</sub>·5H<sub>2</sub>O in 500 ml of water cooled in an ice bath. After stirring for 30 min, aqueous ammonia (25%) was added dropwise until a pH value of 3 to 4 was reached. The white precipitate obtained was collected by centrifugation and washed several times with water. During the latter steps, the color of the precipitates containing antimony changed from white to yellowish. In order to avoid loss of solid material, washing was stopped when the precipitate started to redissolve to a colloidal solution. Subsequently, the precipitate was stirred overnight in about 500 ml of water containing 10 ml of aqueous ammonia (25%). The turbid colloidal solution obtained was further purified by dialysis against 10 liters of aqueous ammonia of pH 9.5–10 (Dialysis tubing: Serva, no. 14146). The resulting transparent colloidal solution was concentrated to 500 ml by using a rotary evaporator, filtered, and finally stabilized by adding 5 ml of aqueous ammonia (25%). The antimony-doped colloids exhibited a yellowish to brownish color, whereas undoped colloids were colorless. Similarly, colloids were prepared by using SbCl<sub>5</sub> instead of SbCl<sub>3</sub>. In this case the colloids remained colorless, too. The molar ratio of tin and antimony in the dialyzed colloids was determined by atomic absorption spectroscopy (AAS) and was found to be equal to the ratio employed in the synthesis.

Powders of nanocrystalline tin dioxide were prepared by removing the solvent of the respective colloidal solution with a rotary evaporator (bath temperature of 50 °C). After drying at 100 °C in air, the residue was ground in a mortar. A por-

tion of each powder sample was additionally heated to 500 °C in air for 1 h in an oven. Upon heating, the brownish color of the doped samples changed to bluish, in accordance with observations made by others.<sup>43,50</sup> Layers of nanocrystalline tin dioxide have been prepared by spin coating at 2500 rpm quartz substrates with the concentrated colloidal solutions. The latter were prepared by adding 1% of glycerin to each colloid and concentrating the colloids by a factor of about 4 using a rotary evaporator. Prior to deposition, 500 μl of 25% ammonia was added under vigorous stirring to the highly viscous solution, which was then passed through a 0.2 μm filter. Spin coating was repeated about ten times, in order to obtain sufficiently thick layers. After each deposition step the layers were heated to 500 °C for 5 min. For comparison, we also prepared layers which were heated to 150 °C only. The thickness of the layers was determined with an alpha-step 200 device (Tencor Instruments). The conductivity of the layers was measured by the standard four-point method.<sup>51</sup>

### B. Transmission electron microscopy and powder x-ray diffraction

High-resolution transmission electron micrographs of the colloids were taken using a Philips CM 300 UT electron microscopy (300 kV acceleration voltage) equipped with a CCD camera (Gatan, model no. 694).

X-ray powder diffraction patterns of nanocrystalline powders were acquired with a Philips Xpert x-ray diffraction (XRD) system (Cu K<sub>α</sub>-radiation).

### C. XANES and EXAFS measurements

Sb *L*-edge XANES measurements of the samples were performed at 300 K in transmission geometry at beamline *E4* of the DORIS storage ring at HASYLAB, DESY (Hamburg, Germany). This beamline is equipped with a Si(111) double crystal monochromator. Higher harmonics were rejected by utilizing a toroidal Au and Ni plane mirror. The samples were prepared by attaching thin homogeneous layers of finely ground nanocrystalline material onto Scotch tape. An Sb metal foil was measured simultaneously with each sample at the Sb *L*<sub>1</sub> edge between 3850 and 4790 eV. Sb<sub>2</sub>O<sub>3</sub> and Sb<sub>2</sub>O<sub>5</sub> reference spectra were taken as model data for Sb<sup>III</sup> and Sb<sup>V</sup>, respectively. The gases used in the three ionization chambers were 110 mbar N<sub>2</sub>, a mixture of 45 mbar Ar with 775 mbar N<sub>2</sub>, and a mixture of 65 mbar Ar with 775 mbar N<sub>2</sub>, respectively. The energy steps across the *L* edges were 0.4 eV at a counting time of 1–2 s/step.

For the analysis of the Sb *L*<sub>1</sub>-edge XANES data, a smooth background function was determined by fitting a spline to the Sn *L*<sub>1</sub> postedge region using the AUTOBK software (V2.61).<sup>52</sup> This background was combined with the Sb *L*<sub>1</sub>-edge XANES spectra at about 4670 eV, extrapolated by a parabolic function beyond the Sb *L*<sub>1</sub> edge and then subtracted. The resulting spectra were finally normalized to the edge jump in the Sb *L*<sub>1</sub>-continuum region.

Sb *K*-edge EXAFS measurements were performed at beamline X1 (RÖMO 2) (HASYLAB, DESY) equipped with a Si(311) double crystal monochromator which was detuned to 60% of the Bragg peak intensity to eliminate higher har-

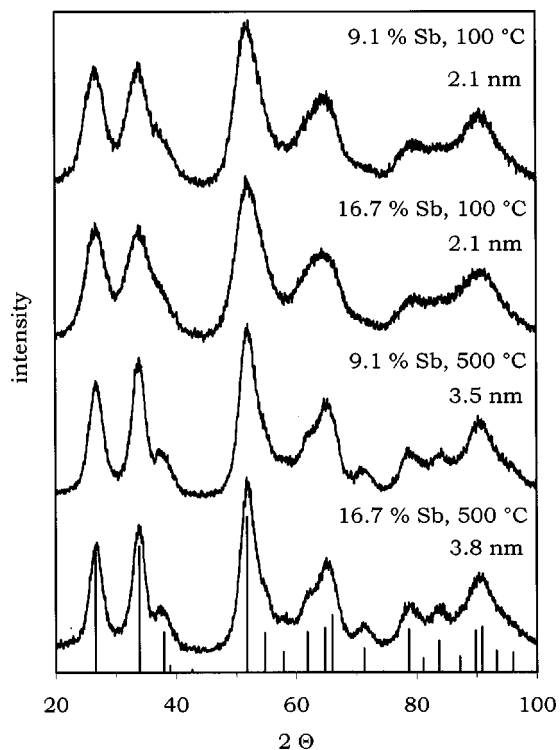


FIG. 1. X-ray powder diffraction patterns of  $\text{SnO}_2$ :Sb nanocrystals doped with 9.1% and 16.7% antimony. Annealing temperatures and resulting particle sizes as labeled.

monics. For the measurements, powders of the nanocrystalline samples as well as powder samples of bulk  $\text{SnO}_2$ ,  $\text{Sb}_2\text{O}_3$ , and  $\text{Sb}_2\text{O}_5$  (Aldrich) were mixed with boron nitride (Aldrich), homogenized by ball milling, and pressed to form stable pellets. Simultaneously with each sample, an Sb foil (Goodfellow) was measured as reference at the Sb  $K$  edge between 30 200 and 31 520 eV. Spectra were taken in transmission mode using three ionization chambers. The first chamber was filled with argon, the second and third with krypton at atmospheric pressure. Energy steps varied from 1 eV in the  $K$  edge region to 4 eV at the end of the scans. Counting time was 2 s/step. Prior to the measurements, the samples were cooled to 5 K using a liquid helium bath cryostat (Oxford).

Background subtraction, normalization, and transfer to  $k$ -space of the Sb  $K$ -edge data were performed following standard procedures using the AUTOBK software (V2.61). Background subtracted data were  $k^2$ -weighted and Fourier transformed between  $k=3.7$  and  $13.0 \text{ \AA}^{-1}$ . The FEFFIT software V2.51<sup>53</sup> was used to fit the data in real space by means of theoretical backscattering amplitudes and phases which were calculated by FEFF5.<sup>54</sup> Three shells were used to fit the data in the region  $r=1.0$ – $4.0 \text{ \AA}$  to describe the nearest neighbor Sb–O shell and two outer Sb–metal coordination spheres; 19 independent data points were fitted by 9 variables.

### III. RESULTS AND DISCUSSION

#### A. X-ray powder diffraction pattern and TEM images

Figure 1 shows the x-ray diffraction patterns of doped nanocrystalline powders after heating to 100 °C and 500 °C,

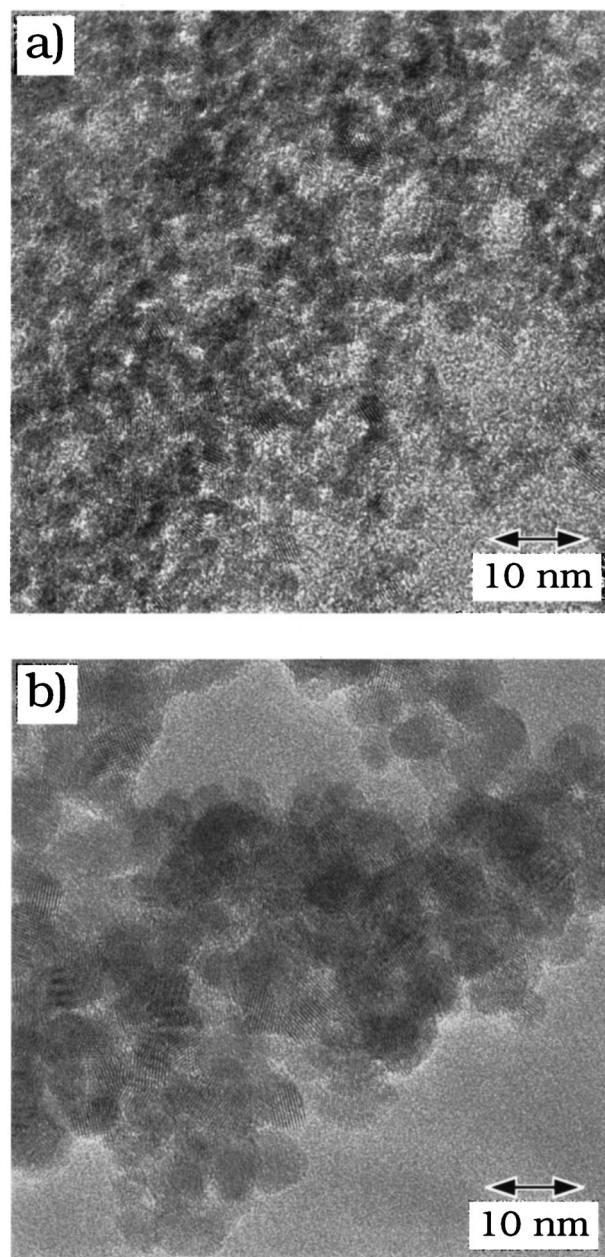


FIG. 2. High-resolution TEM images of  $\text{SnO}_2$ :Sb nanocrystals (Sb 9.1%) (a) after drying at 100 °C, (b) after subsequent heating to 500 °C.

respectively. The peak positions agree well with the bulk  $\text{SnO}_2$  (cassiterite) reflections (depicted schematically at the bottom of Fig. 1), indicating the same rutile lattice structure. No other phase but cassiterite is observed in the x-ray diffraction patterns. The width of the reflections is considerably broadened, indicating a small crystalline domain size. This can be roughly quantified using the Debye–Scherrer formula for spherical particles. Analysis of the (110) peaks yields the domain sizes noted in the figure. The extent of particle growth upon heating to 500 °C is affected by the presence of antimony. Heating of the initially 2 nm large particles containing no antimony yields colloids of about 9 nm in diameter, whereas doped particles (9.1% Sb as well as 16.7% Sb) grow to only about 3.5 to 4 nm. A similar depression of particle growth has been frequently observed in doped  $\text{SnO}_2$  nanocrystals (see, for instance Ref. 46).

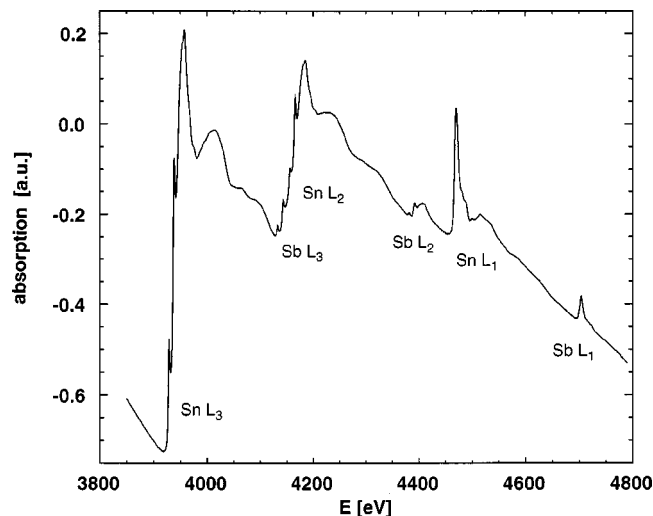


FIG. 3. XANES raw data at the Sn and Sb *L* edges of SnO<sub>2</sub>:Sb (16.7% Sb, 500 °C). Sn *L*<sub>3,2,1</sub> = 3929, 4157, 4465 eV; Sb *L*<sub>3,2,1</sub> = 4132, 4382, 4698 eV.

TEM images of doped SnO<sub>2</sub> colloids heated to 100 °C and 500 °C, respectively, are shown in Fig. 2. Lattice fringes are observed for most particles, proving their high crystallinity. The micrographs show particles ranging from 2 to 3 nm in diameter for colloids dried at 100 °C, and particles of about 4 to 6 nm after heating to 500 °C, roughly in accord with the XRD data.

### B. Valence state and coordination of antimony by means of XANES and EXAFS

Figure 3 displays the x-ray absorption raw data of one sample (16.7% Sb, 500 °C) in the energy region between 3850 and 4790 eV. After background subtraction and normalization (see Sec. II) the shape of the Sb *L*<sub>1</sub>-edge spectrum of each sample was compared with an Sb<sub>2</sub>O<sub>3</sub> and Sb<sub>2</sub>O<sub>5</sub> reference spectrum (solid lines in Fig. 4, top), respectively. Apparently, the position of the Sb *L*<sub>1</sub> edge is rather sensitive to the oxidation state of antimony. Both in Sb<sup>III</sup> and Sb<sup>V</sup> oxide, electronic transitions occur from the Sb 2*s*<sub>1/2</sub> level into unoccupied *p*-like density of states derived from atomic 5*p* states. The apparent sensitivity of the XANES data in Fig. 4, top to the Sb valence state originates therefore in the presence or lack of the 5*s* electrons in Sb<sup>III</sup>/Sb<sup>V</sup> oxide, respectively. This assumes that the edge position is dominated by the Sb valence state and that next-nearest neighbor scattering contributions which mostly influence postedge features are of minor importance. In this case, the Sb<sup>III</sup>/Sb<sup>V</sup> ratio in the samples can be determined by fitting Sb *L*<sub>1</sub>-edge XANES data with a linear combination of the Sb<sub>2</sub>O<sub>3</sub> and Sb<sub>2</sub>O<sub>5</sub> reference spectra (broken lines in Fig. 4). In addition, the fits were also performed for the derivatives of the absorption spectra (Fig. 5) in order to prove a correct data normalization. As shown in Figs. 4 and 5, the linear combinations reproduce the experimentally obtained spectra very well. The result of this analysis, i.e., the relative amount of Sb<sup>III</sup> and Sb<sup>V</sup> in each sample, is listed in Table I. By comparing the results in Table I, it is evident that, if Sb<sup>III</sup> is used in the synthesis, there is a strong tendency to form Sb<sup>V</sup>, irrespective

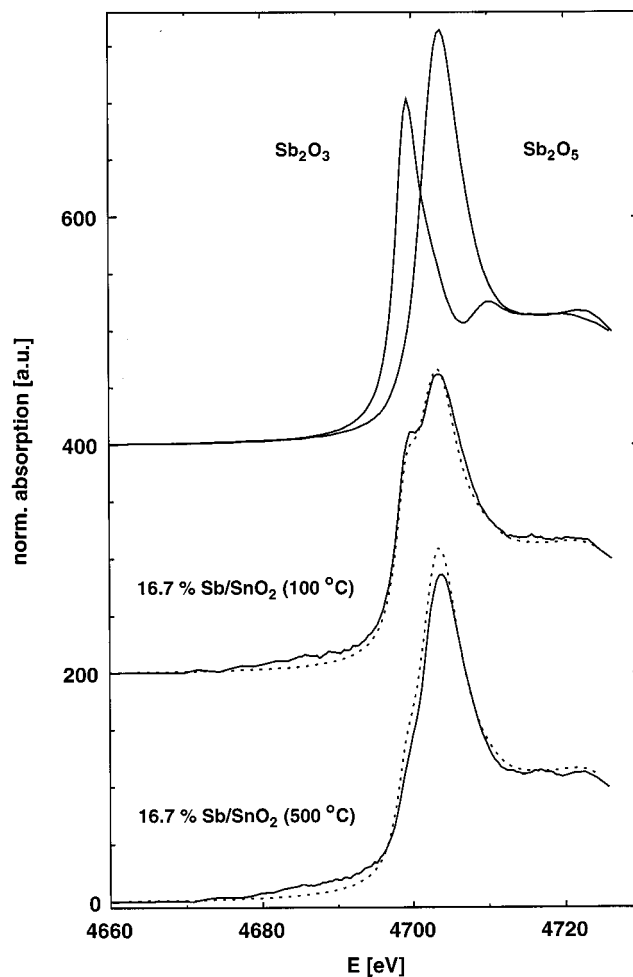


FIG. 4. Normalized XANES spectra at the Sb *L*<sub>1</sub> edge. Upper part: Sb<sub>2</sub>O<sub>3</sub> and Sb<sub>2</sub>O<sub>5</sub> reference compounds. Middle and lower part: Experimental data (solid) of SnO<sub>2</sub>:Sb(16.7%) after heating to 100 °C and 500 °C, respectively. A linear combination fit (dotted) by means of the above reference spectra was applied to evaluate the relative amount of Sb<sup>III</sup> and Sb<sup>V</sup> in the doped nanocrystals.

of the doping level. The values in the first column show that already after drying at 100 °C more than half of the initially employed Sb<sup>III</sup> is oxidized. In contrast, if Sb<sup>V</sup> is used in the synthesis, almost no reduction to Sb<sup>III</sup> is observed upon drying at 100 °C and the sample remains almost colorless, whereas all samples containing antimony in both oxidation states exhibit a strong yellowish to brownish color. In a previous study using a similar preparation of SnO<sub>2</sub>:Sb, this color has been attributed to an intervalence transition.<sup>47</sup> Since the yellowish coloration already develops during the synthesis, the oxidation of antimony is likely to take place at early stages of particle formation and crystallization. In fact, the driving force for the oxidation process is remarkably strong. The data in Table I for the samples dried at 100 °C prove that slow oxidation takes place even at room temperature. This indicates that (hydrated) Sb<sub>2</sub>O<sub>3</sub> is not the main product after precipitation with ammonia, as the oxidation state of antimony in this substance is known to be stable at room temperature.<sup>55</sup> Independent of the doping level and the antimony precursor used in the synthesis, the system finally reaches an Sb<sup>III</sup>/Sb<sup>V</sup> ratio of roughly 1 to 3 (see Table I).

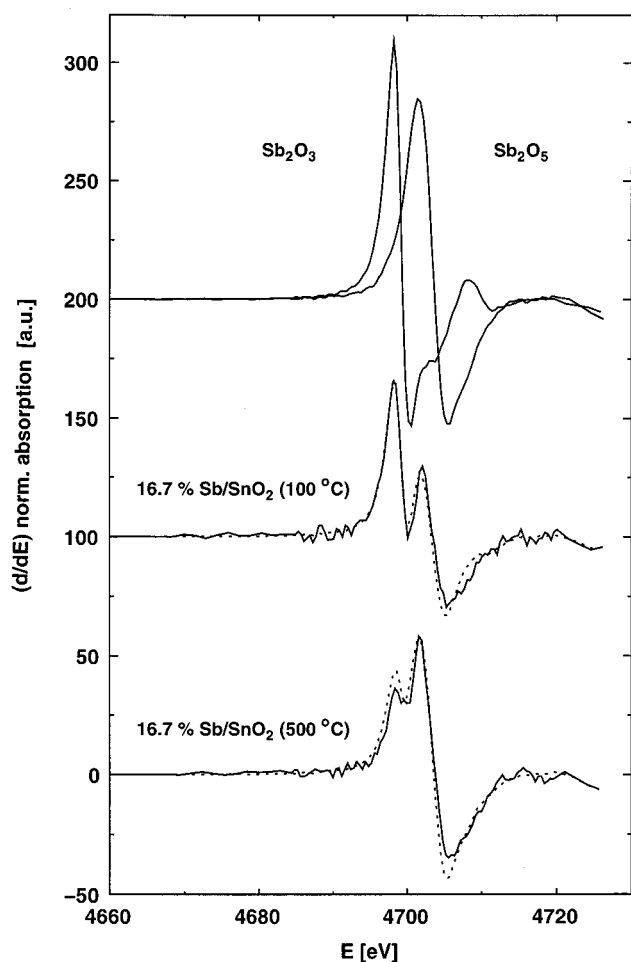


FIG. 5. Derivative spectra of the data shown in Fig. 4.

This ratio is not encountered in any of the known oxides of antimony, i.e.,  $\text{Sb}_2\text{O}_3$ ,  $\text{Sb}_2\text{O}_4$ ,  $\text{Sb}_6\text{O}_{13}$ , and  $\text{Sb}_2\text{O}_5$ .<sup>56</sup> Moreover, none of the crystalline phases of any of the various antimony oxides is detected in our XRD patterns.

In order to probe the local atomic environment of antimony in our samples, we studied the extended x-ray absorption fine structure (EXAFS) of the Sb  $K$  edge at 5 K. The solid lines in Fig. 6 display the normalized,  $k^2$ -weighted Sb  $K$ -edge EXAFS data  $k^2\chi^{(k)}$  and the magnitude of their Fourier transforms of nanocrystalline  $\text{SnO}_2\text{:Sb}$  after heating to 100 °C and 500 °C, respectively. Fits to the experimental data assuming three neighboring shells of antimony in tin

dioxide (Sb–O, Sb–Sn/Sb, and Sb–Sn/Sb) are shown as broken lines in the same figure. The numerical results of all fits are summarized in Table II. Since Sb and Sn are neighbors in the periodic table and, consequently, exhibit very similar scattering properties, they cannot be distinguished as back-scatterers in EXAFS experiments. As was proven, fits with Sb instead of Sn in the second and third shell around Sb gave similar results within the experimental error. Note that other fitting models than the one shown in Table II (including for instance different coordination shells for  $\text{Sb}^{\text{III}}$  and  $\text{Sb}^{\text{V}}$ ) yielded no reasonable description of the data.

The first strong peak around 2.0 Å in the Fourier transforms corresponds to the Sb–O coordination shell, which is very similar in all samples and is in accordance with literature values for the nearest-neighbor distances in  $\text{SnO}_2$  and various antimony oxides (Table II). Therefore, the first coordination shell by itself cannot be used to decide whether antimony is part of an antimony oxide grain or is doped into the tin dioxide lattice. Inspection of the higher neighbor shell distances, however, reveals that the experimentally observed distances (Table II) agree very well with the metal–metal distances in  $\text{SnO}_2$ . This is a very strong indication that antimony occupies tin sites in the tin dioxide lattice of the particles.

The contraction of the Sb nearest-neighbor distance (Sb–O) with respect to bulk  $\text{SnO}_2$  indicates local distortions of the Sb–O polyeder. The latter would be expected for the incorporation of  $\text{Sb}^{\text{V}}$  ions which, in sixfold coordination, have a smaller ionic radius ( $r=0.60$  Å) than the tin ions ( $r=0.69$  Å). The observed increase of the mean-square relative displacement ( $\sigma_1^2$  in Table II) reflects an increased lattice distortion with increasing doping level. Next-nearest neighbor distances (i.e., between Sb and Sb/Sn) do not show a contraction as was observed in Cu-doped  $\text{SnO}_2$  by others,<sup>46,57</sup> probably because of the stronger Coulomb interactions between Sb and the Sn atoms of its environment. Incorporation of the antimony into the tin dioxide lattice may also explain the strong tendency to form  $\text{Sb}^{\text{V}}$  which may be built more easily into the lattice than the large  $\text{Sb}^{\text{III}}$  ion ( $r=0.76$  Å). In fact, an investigation of  $\text{SnO}_2\text{:Sb}$  by Mössbauer spectroscopy indicated the presence of  $\text{Sb}^{\text{V}}$  ions in roughly octahedral sites, together with  $\text{Sb}^{\text{III}}$  at surface sites or grain boundaries.<sup>33</sup> Since the particle size and, consequently, the surface-to-volume ratio of our nanocrystals is similar in all doped samples (even after heating to 500 °C, see above),

TABLE I. Relative amount of  $\text{Sb}^{\text{III}}$  and  $\text{Sb}^{\text{V}}$  determined from the Sb  $L_1$ -edge XANES spectra for different preparation and sample conditions of the  $\text{SnO}_2\text{:Sb}$  nanoparticles.

Oxidation state and relative amount of antimony chloride employed in synthesis		Preparation conditions	
		Drying at 100 °C Percentage $\text{Sb}^{\text{III}}/\text{Sb}^{\text{V}}$	Drying and subsequent annealing at 500 °C Percentage $\text{Sb}^{\text{III}}/\text{Sb}^{\text{V}}$
9.1% $\text{Sb}^{\text{III}}$	(a) after 1 week at 20 °C	35/65	28/72
	(b) after 6 months at 20 °C	22/78	28/72
16.7% $\text{Sb}^{\text{III}}$	(c) after 1 week at 20 °C	50/50	23/77
	(d) after 6 months at 20 °C	21/79	21/79
16.7% $\text{Sb}^{\text{V}}$	(e) after 1 week at 20 °C	9/91	24/76

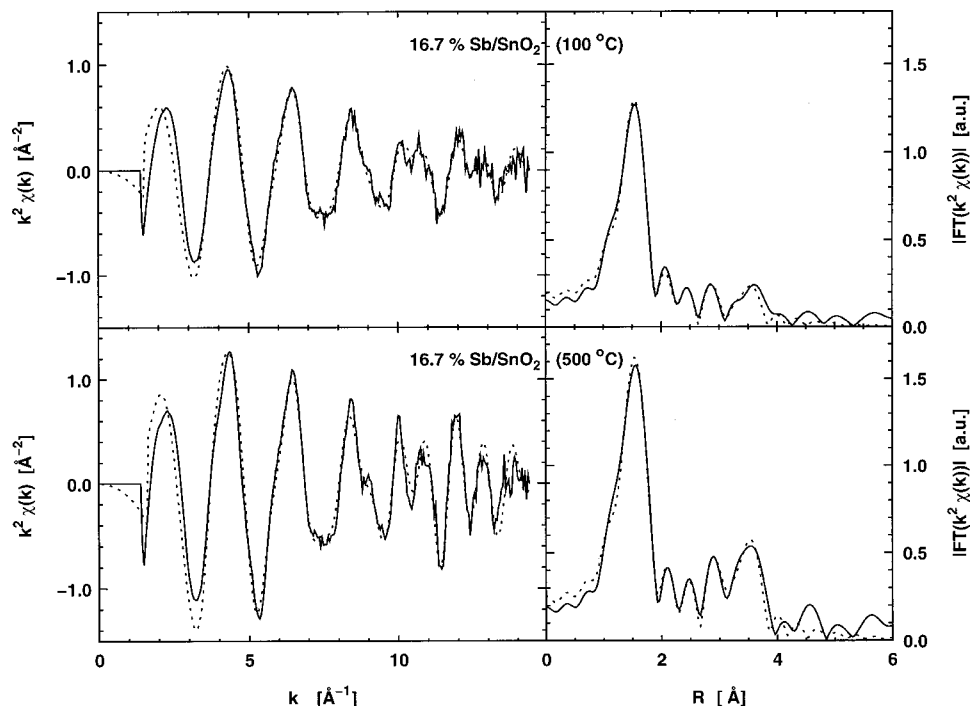


FIG. 6. Solid lines: Sb *K*-edge EXAFS functions  $k^2\chi(k)$  (left part) and corresponding Fourier transforms (right part) for nanocrystalline SnO<sub>2</sub>:Sb at 5 K. Broken lines: Fits to the experimental curves.

this observation may also explain why the final Sb<sup>III</sup>/Sb<sup>V</sup> ratio is almost identical in all our samples. Moreover, this picture is consistent with our observation that the coordination number  $N_1$  of the Sb–O shell in all our samples is smaller than the expected value of 6 for octahedral coordination. Therefore, some of the antimony ions must be located at the surface of the nanocrystals.

From the TEM micrographs and the XRD data, it is evident that the particles grow weakly upon annealing at 500 °C. The slightly enhanced particle size and an improved crystallinity is reflected in the observed increase of the coordination numbers (Table II) of the third shell (Sb–Sn) and the reduction of the corresponding mean-square relative displacement (MSRD) after annealing. Table II also shows that the coordination numbers for the higher neighbor shells are lower than in the corresponding bulk material. This deviation

is always observed for crystalline nanoparticles<sup>58–61</sup> and is in part caused by the large surface-to-volume ratio in these materials, which reduces the mean value of the coordination numbers of higher neighbor shells. An interpretation of the measured coordination numbers  $N_2$  and  $N_3$  (Table II) with respect to the question of whether the Sb atoms are predominantly incorporated at the surface of the nanoparticle or randomly substitute Sn within the whole particle would require a model assumption for nanocrystal shape and faceting. Note that in this specific case where EXAFS cannot distinguish between Sn and Sb backscatterers, no direct information is available from the data. However, the low values of  $N_2$  and  $N_3$  are consistent with a preferred Sb occupation of sites at the nanocrystal surface. This may also be the reason for the observed hindering of particle growth during annealing of the doped particles with respect to the undoped ones (see the

TABLE II. Fitting results of Sb *K*-edge EXAFS data.

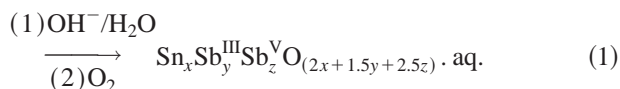
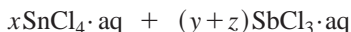
Sample		1st shell: Sb–O			2nd shell: Sb–Sn (Sb)			3rd shell: Sb–Sn (Sb)			
Sb doping	Temp.	$E_0$	$N_1$	$R_1$ [Å]	$\sigma_1^2$ [ $10^{-3}$ Å <sup>2</sup> ]	$N_2$	$R_2$ [Å]	$\sigma_2^2$ [ $10^{-3}$ Å <sup>2</sup> ]	$N_3$	$R_3$ [Å]	$\sigma_3^2$ [ $10^{-3}$ Å <sup>2</sup> ]
9.1%	100 °C	10.1(17)	4.3(5)	2.00(2)	2.2(11)	0.9(6)	3.20(2)	2.0(12)	1.5(10)	3.71(2)	2.0(12)
	500 °C	10.5(14)	4.9(6)	1.98(2)	2.4(10)	1.1(5)	3.20(2)	1.4(10)	2.4(10)	3.72(2)	1.4(10)
16.7%	100 °C	8.3(10)	4.1(3)	1.98(2)	3.4(8)	0.7(4)	3.20(2)	3.1(10)	1.3(6)	3.70(2)	3.0(10)
	500 °C	10.3(10)	5.4(4)	2.00(2)	3.8(8)	0.9(4)	3.20(2)	1.5(9)	2.4(7)	3.73(2)	1.5(9)
References (Lit. values)											
SnO <sub>2</sub>			6	2.05		2	3.19		8	3.71	
Sb <sub>2</sub> O <sub>3</sub>			3	1.98		3	3.62		6	3.94	
Sb <sub>2</sub> O <sub>5</sub>			6	1.89–2.10		1+3	3.24, 3.54		2+2	3.67, 3.78	
Sb <sub>2</sub> O <sub>4</sub>				1.86–2.62			3.41–3.63			3.74–4.02	

XRD results). Furthermore, Table II shows an increased width of the bond-length distributions with respect to the bulk due to the surface-induced deformation of the nanocrystal's lattice. This is often observed for nanoparticles.

### C. Two-step formation model for *n*-conducting SnO<sub>2</sub>:Sb nanocrystals

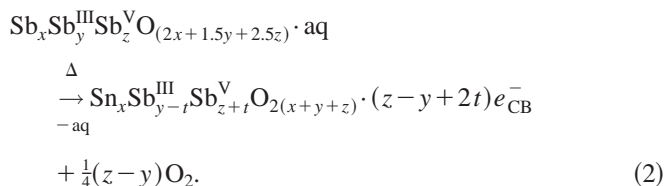
In this section, a quantitative two-step reaction model of the formation of *n*-conductive SnO<sub>2</sub>:Sb is presented. It is based on the requirement of charge balance in the sample during (i) the low-temperature synthesis of the doped nanocrystals, and (ii) the heating process. The results of the previous section, in particular the Sb valence state determination, enable a quantitative evaluation.

Before heating to 500 °C, the samples show neither a plasma absorption in the red-to-IR region nor are they conductive. Layers of the nanoparticles deposited onto glass substrates by spin coating exhibit a sheet resistance of  $>2 \cdot 10^{10} \Omega/\text{sq}$ . Obviously, the mixed oxides obtained after drying at 100 °C contain no conduction band electrons and their composition is given by  $x\text{SnO}_2 \cdot (y/2)\text{Sb}_2^{\text{III}}\text{O}_3 \cdot (z/2)\text{Sb}_2^{\text{V}}\text{O}_5 \cdot \text{aq}$  or, using a different notation,  $\text{Sn}_x\text{Sb}_y^{\text{III}}\text{Sb}_z^{\text{V}}\text{O}_{(2x+1.5y+2.5z)} \cdot \text{aq}$ . The reaction leading to the *nonconductive* produce may then be written as



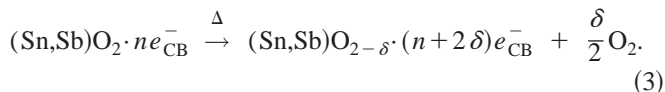
Except for the special case where the product contains equal amounts of Sb<sup>III</sup> and Sb<sup>V</sup>, the requirement of charge balance causes the metal-to-oxygen ratio in the mixed oxide to slightly deviate from 1:2. For the samples (a)–(d) dried at 100 °C with an Sb<sup>III</sup>/Sb<sup>V</sup> ratio from 1:1 to 1:4 (Table I), a metal-to-oxygen ratio ranging from 1:2.00 to 1:2.05 is expected [e.g., 1:2.01 for sample (a), 100 °C]. It is emphasized that all samples dried at 100 °C remain nonconductive also after aging.

Upon heating to 500 °C, the doped samples change their color to bluish and become electrically conductive. The sheet resistance of nanoparticle films deposited by spin coating drops to  $\leq 1000 \Omega/\text{sq}$ , i.e., by at least 7 orders of magnitude, although our samples contain more antimony than is usually employed for highly conductive bulk films. The strong decrease of the resistivity is commonly explained by the formation of an *n*-conductive oxide, the blue color being attributed to the plasma absorption of free conduction band electrons.<sup>31,32,50</sup> Following standard theory, the donor ions in an *n*-conductive oxide are expected to occupy the sites of the host metal ion. In fact, the XRD data of bulk single crystals of SnO<sub>2</sub> doped with 4% antimony indicate that the antimony ions occupy tin sites of the host lattice.<sup>62</sup> Since each donor ion replaces one metal ion of the host, doping with antimony alone leaves the ratio between cations (tin+antimony) and anions (oxygen) unchanged, i.e., at its value of the undoped host, 1:2 in the case of SnO<sub>2</sub>. Following the requirement of charge balance in the doped oxide, the formation of *n*-conductive SnO<sub>2</sub>:Sb is then given by the following reaction scheme:



Here,  $e_{\text{CB}}^-$  indicates the number of conduction band electrons in the *n*-conductive oxide. The XANES results (Table I) allow the determination of the parameters  $y$  and  $z$  as well as the change of the antimony valence state, given by parameter  $t$ .

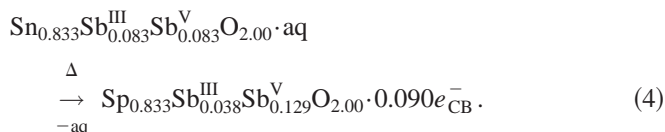
In reaction (2), oxygen released from the lattice is assumed to form molecular oxygen and the formation of oxygen deficiencies is neglected. However, bulk SnO<sub>2</sub> is well-known to form oxygen deficiencies.<sup>63</sup> Moreover, the oxygen-to-metal ratio in SnO<sub>2</sub> films prepared by spray coating at 500 °C is reported<sup>34</sup> to be 1.96. Oxygen vacancies in bulk SnO<sub>2</sub> are known to increase the *n*-conductivity of tin dioxide, since they form donor states with low ionization energy, similar to antimony atoms.<sup>63</sup> Reaction scheme (2) can be extended easily to include oxygen deficiencies, as follows:



Hence, each oxygen vacancy provides two electrons to the conduction band in accordance with standard theory.

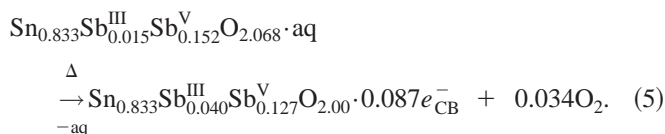
In the following, we discuss reaction scheme (2) with respect to our XANES results compiled in Table I. For simplicity, and since we heated our samples in air, i.e., under oxidizing conditions, the formation of oxygen deficiencies is neglected.

If the tin dioxide particles contain 16.7% of antimony and the educt contains equal amounts of Sb<sup>III</sup> and Sb<sup>V</sup> [i.e., case (c) in Table I], we can describe the formation of the *n*-conductive phase at 500 °C as



In this case, the oxygen content of the lattice remains completely unchanged. All conduction band electrons are created by the oxidation state change of a fraction of the antimony ions.

On the other hand, if a product as above is produced from an Sb<sup>V</sup> source [case (e) in Table I], the reaction scheme is



Thus, in this case each 3.5 nm particle (containing about 600 SnO<sub>2</sub> molecules) is expected to release about 40 oxygen atoms during the formation of the *n*-conductive oxide. Interestingly, most authors describing the preparation of conductive SnO<sub>2</sub>:Sb films at temperatures around 500 °C used an Sb<sup>III</sup> source, although in single crystals of SnO<sub>2</sub>:Sb antimony is known to have the oxidation state 5+. In fact, we observe

that the conductivity of particle layers is lower if Sb<sup>V</sup> is used in the colloid synthesis instead of Sb<sup>III</sup>. A possible explanation is that at 500 °C and in the absence of any reducing agent the release of oxygen as given by reaction (5) does not reach completion, resulting in a product with a higher oxygen content and a smaller number of free electrons as given by scheme (5).

For all other cases listed in Table I, the amount of oxygen released during reaction (2) lies between the two extreme cases discussed above. Note that for a given Sb<sup>III</sup>/Sb<sup>V</sup> ratio the change in oxygen content is smaller at lower doping levels.

The results indicate that the formation of *n*-conductive SnO<sub>2</sub>:Sb follows a two-step mechanism. The XRD and EXAFS data clearly show that already after drying at 100 °C nanoparticles are formed which exhibit the (presumably distorted) rutile phase (cassiterite). Moreover, the EXAFS results reveal that the antimony is incorporated into the cassiterite lattice at moderate temperature. Incorporation of antimony is accompanied by a change of the valence state of antimony from 3+ to 5+. The latter process proceeds slowly even at room temperature. Thus, the first step at low temperature yields rutile phase SnO<sub>2</sub>:Sb nanoparticles exhibiting no electrical conductivity and a yellowish color. Electrical conductivity is not observed until the particles are heated to elevated temperatures, i.e., 500 °C in our experiments. The structural changes accompanying this insulator-to-conductor transition are remarkably small. According to scheme (2), the oxygen content is expected to change, but this small decrease in the EXAFS mean coordination number is by far overcompensated by the occurring particle growth (Table II). The decrease of the EXAFS Debye–Waller factors after heating indicates an enhanced crystallinity in the vicinity of the antimony ions; however, this may at least partly be explained by growth of the SnO<sub>2</sub>:Sb particles upon heating (see Fig. 1). According to reaction scheme (2), one mol Sn<sub>0.91</sub>Sb<sub>0.09</sub>O<sub>2</sub> containing antimony in an Sb<sup>III</sup>/Sb<sup>V</sup> ratio of 1:3 should carry 45 mmol of conduction band electrons, corresponding to an electron density in the lattice of 1.2 · 10<sup>21</sup> cm<sup>-3</sup>. Similarly, an electron density of 2.3 · 10<sup>21</sup> cm<sup>-3</sup> is expected in the case of Sn<sub>0.83</sub>Sb<sub>0.17</sub>O<sub>2</sub> having an Sb<sup>III</sup>/Sb<sup>V</sup> ratio of 1:3. However, others have shown that the electron density in SnO<sub>2</sub>:Sb films prepared by dip coating is somewhat lower for doping levels in this range, i.e., about 0.3 · 10<sup>21</sup> cm<sup>-3</sup> to 0.8 · 10<sup>21</sup> cm<sup>-3</sup>.<sup>64</sup> This indicates that the compensation phenomenon<sup>34,64</sup> between Sb<sup>III</sup> and Sb<sup>V</sup> alone cannot completely account for the low electron densities observed. Hence, either the reaction from the nonconductive to the *n*-conductive oxide does not reach completion at higher doping levels or an increasing number of electrons is trapped in deep sites, e.g., in surface sites. At present, we are not able to distinguish between these two possibilities. In order to verify the first model, it would be desirable to directly measure the oxygen-to-metal ratio in each sample, e.g., by XPS or by chemical analysis. However, this is hampered by the fact that the surface of tin dioxide nanoparticles is saturated by OH species and H<sub>2</sub>O,<sup>47</sup> preventing an exact analysis of the oxygen content of the nanocrystalline particle core. On the other hand, the nature of trap states cannot be

deduced from the model given above, since the latter is solely based on the requirement of charge neutrality in each compound without making any assumption on the explicit nature of electronic states. Due to the latter, however, our analysis applies independently of the exact nature of the donor states, for which different models have been given.<sup>33,38</sup>

#### IV. SUMMARY

Colloidal solutions and powders of rutile-type antimony-doped SnO<sub>2</sub> nanocrystals with a particle diameter of about 2–6 nm have been prepared by the coprecipitation method. Whereas the XRD data only show that antimony does not form a separate crystalline phase, Sb *K*-edge EXAFS measurements at 5 K actually prove that the antimony is incorporated into the tin dioxide lattice of samples dried and annealed at 100 °C and 500 °C, respectively. A contraction of the Sb nearest-neighbor distance with respect to SnO<sub>2</sub> indicates local distortions of the Sb–O polyeder. Sb *L*<sub>1</sub>-edge XANES measurements of the samples reveal that SnO<sub>2</sub> nanoparticles doped with 9.1% and 16.7% antimony both exhibit a high amount of Sb<sup>V</sup> before annealing at 500 °C in air, although Sb<sup>III</sup> was used in the synthesis. Therefore, in the first low-temperature reaction step, incorporation of antimony in the host lattice as well as oxidation occurs, but electrical conductivity is not observed. *n*-conductivity is only developed after annealing the particles at 500 °C. During this second reaction step the relative amount of Sb<sup>V</sup> in our 2–6 nm particles is stabilized at an Sb<sup>III</sup>/Sb<sup>V</sup> ratio of about 1 to 3. Despite the strong effect of annealing on the conductivity, the structural changes observed by Sb *K*-edge EXAFS measurements accompanying the insulator-to-conductor transition are relatively small.

#### ACKNOWLEDGMENTS

We thank J. Ludwig and Dr. Klaska from the Mineralogisch-Petrographisches Institut of the University of Hamburg for the measurement of the powder x-ray diffraction patterns, and S. Naused and A. Kornowski for acquiring transmission electron micrographs.

<sup>1</sup>A. Henglein, *Top. Curr. Chem.* **143**, 113 (1988).

<sup>2</sup>A. Henglein, *Chem. Rev.* **89**, 1861 (1989).

<sup>3</sup>L. E. Brus, *Appl. Phys. A: Solids Surf.* **53**, 465 (1991).

<sup>4</sup>Y. Wang and N. Herron, *J. Phys. Chem.* **95**, 525 (1991).

<sup>5</sup>H. Weller, *Angew. Chem. Int. Ed. Engl.* **32**, 41 (1993).

<sup>6</sup>H. Weller, *Adv. Mater.* **5**(2), 88 (1993).

<sup>7</sup>H. Weller and A. Eychmüller, *Advances in Photochemistry, Volume 20*, edited by D. C. Neckers, D. H. Volman, and G. v. Bünau (Wiley, New York, 1995), p. 165.

<sup>8</sup>A. P. Alivisatos, *J. Phys. Chem.* **100**, 13226 (1996).

<sup>9</sup>A. P. Alivisatos, *Science* **271**, 933 (1996).

<sup>10</sup>W. G. Becker, A. J. Bard, *J. Phys. Chem.* **87**, 4888 (1983).

<sup>11</sup>D. Gallagher, W. E. Heady, J. M. Racz, and R. N. Bhargava, *J. Cryst. Growth* **138**, 970 (1994).

<sup>12</sup>R. N. Bhargava, D. Gallagher, X. Hong, and A. Nurmikko, *Phys. Rev. Lett.* **72**, 416 (1994).

<sup>13</sup>Y. L. Soo, Z. H. Ming, S. W. Huang, Y. H. Kao, R. N. Bhargava, and D. Gallagher, *Phys. Rev. B* **50**(11), 7602 (1994).

<sup>14</sup>K. Sooklal, B. S. Cullum, S. M. Angel, and C. J. Murphy, *J. Phys. Chem.* **100**, 4551 (1996).

<sup>15</sup>G. Counio, S. Esnouf, T. Gacoin, and J.-P. Boillot, *J. Phys. Chem.* **100**, 20021 (1996).

<sup>16</sup>L. Levy, J. F. Hochepped, and M. P. Pileni, *J. Phys. Chem.* **100**, 18322 (1996).

- <sup>17</sup>G. Counio, T. Gacoin, and J.-P. Boilot, *J. Phys. Chem. B* **102**, 5257 (1998).
- <sup>18</sup>T. Schmidt, G. Müller, L. Spanhel, K. Kerkel, and A. Forchel, *Chem. Mater.* **10**, 65 (1998).
- <sup>19</sup>K. Riwozki and M. Haase, *J. Phys. Chem. B* **102**, 10129 (1998).
- <sup>20</sup>P. Mulvaney, F. Grieser, and D. Meisel, *Langmuir* **6**, 567 (1990).
- <sup>21</sup>Z. M. Jarzebski, J. P. Marton, *J. Electrochem. Soc.* **123**(9), 299C (1976).
- <sup>22</sup>Z. M. Jarzebski, J. P. Marton, *J. Electrochem. Soc.* **123**(10), 333C (1976).
- <sup>23</sup>Landolt-Börnstein, in *Numerical Data and Functional Relationships in Science and Technology*, New Series, Group III: Vol. 17 F (Springer, Berlin, 1983).
- <sup>24</sup>K. L. Chopra, S. Major, and D. K. Pandya, *Thin Solid Films* **102**, 1 (1983).
- <sup>25</sup>J.-M. J. Herrmann, J.-L. Portefaix, M. Forissier, F. Figueras, and P. Pichat, *J. Chem. Soc., Faraday Trans. 1* **1**, 1346 (1979).
- <sup>26</sup>H. Koch, *Phys. Status Solidi* **3**, 1059 (1963).
- <sup>27</sup>E. Shanthi, V. Dutta, A. Banerjee, and K. L. Chopra, *J. Appl. Phys.* **51**, 6243 (1980).
- <sup>28</sup>A. L. Dawar and J. C. Joshi, *J. Mater. Sci.* **19**, 1 (1984).
- <sup>29</sup>G. Frank, E. Kauer, and H. Köstlin, *Thin Solid Films* **77**, 107 (1981).
- <sup>30</sup>I. Hamberg and C. G. Granqvist, *J. Appl. Phys.* **60**, R123 (1986).
- <sup>31</sup>P. Grosse, *Freie Elektronen in Festkörpern* (Springer, Berlin, 1979).
- <sup>32</sup>Ch. Kittel, *Introduction to Solid State Physics*, 6th ed. (Wiley, New York, 1986).
- <sup>33</sup>F. J. Berry and B. J. Laundy, *J. Chem. Soc. Dalton Trans.* **1981**, 1442.
- <sup>34</sup>M. Kojina, H. Kato, and M. Gatto, *Philos. Mag. B* **68**(2), 215 (1993).
- <sup>35</sup>J. R. Christie, D. Taylor, and C. C. McCain, *J. Chem. Soc., Faraday Trans. 1* **72**, 334 (1976).
- <sup>36</sup>D. L. Timm and D. S. Galbay, *Trans. Faraday Soc.* **67**, 2782 (1971).
- <sup>37</sup>D. R. Pyke, R. Reid, and R. J. D. Tilley, *J. Chem. Soc., Faraday Trans. 1* **76**, 1174 (1981).
- <sup>38</sup>F. J. Berry and B. C. Greaves, *J. Chem. Soc. Dalton Trans.* **1981**, 2447.
- <sup>39</sup>P. A. Cox, R. G. Egdell, C. Harding, W. R. Patterson, and P. T. Tavener, *Surf. Sci.* **123**, 179 (1982).
- <sup>40</sup>Y. M. Cross and D. R. Pyke, *J. Catal.* **58**, 61 (1979).
- <sup>41</sup>Y. Boudeville, F. Figueras, M. Forissier, J.-L. Portefaix, and J. C. Vedrine, *J. Catal.* **58**, 52 (1979).
- <sup>42</sup>C. Terrier, J. P. Chatelon, R. Berjoan, and J. A. Roger, *Thin Solid Films* **263**, 37 (1995).
- <sup>43</sup>V. Briois, C. V. Santilli, S. H. Pulcinelli, and G. E. S. Brito, *J. Non-Cryst. Solids* **191**, 17 (1995).
- <sup>44</sup>G. E. S. Brito, V. Briois, S. H. Pulcinelli, and C. V. Santilli, *J. Sol-Gel Sci. Technol.* **8**, 269 (1997).
- <sup>45</sup>G. E. S. Brito, S. J. L. Ribeiro, V. Briois, J. Dexpert-Ghys, C. V. Santilli, and S. H. Pulcinelli, *J. Sol-Gel Sci. Technol.* **8**, 261 (1997).
- <sup>46</sup>S. R. Davis, A. V. Chadwick, and J. D. Wright, *J. Phys. Chem. B* **101**, 9901 (1997).
- <sup>47</sup>C. A. Vincent and D. G. C. Weston, *J. Electrochem. Soc.* **119**(4), 519 (1972).
- <sup>48</sup>Z. Crnjak-Orel, B. Orel, M. Hodosecek, and V. Kaucic, *J. Mater. Sci.* **27**, 313 (1992).
- <sup>49</sup>B. Orel, U. Lavrencic-Stangar, Z. Crnjak-Orel, P. Bukovec, and M. Kosec, *J. Non-Cryst. Solids* **167**, 272 (1994).
- <sup>50</sup>G. Boschloo and D. Fitzmaurice, *J. Phys. Chem. B* **103**, 3093 (1999).
- <sup>51</sup>L.-J. van der Pauw, *Philips Res. Rep.* **13**, 1 (1958).
- <sup>52</sup>M. Newville, P. Livins, Y. Yacoby, J. J. Rehr, and E. A. Stern, *Phys. Rev. B* **47**, 14126 (1993).
- <sup>53</sup>E. A. Stern, M. Newville, B. Ravel, Y. Yacoby, and D. Haskel, *Physica B* **208–209**, 154 (1995).
- <sup>54</sup>J. J. Rehr, R. C. Albers, and S. I. Zabinsky, *Phys. Rev. Lett.* **69**, 3397 (1992).
- <sup>55</sup>A. Simon and E. Thaler, *Z. Chem.* **162**, 253 (1927).
- <sup>56</sup>D. J. Stewart, O. Knop, C. Ayasse, and F. W. D. Woodhams, *Can. J. Chem.* **50**, 690 (1972).
- <sup>57</sup>C. V. Santilli, S. H. Pulcinelli, G. E. S. Brito, and V. Briois, *J. Phys. Chem. B* **103**, 2660 (1999).
- <sup>58</sup>M. A. Marcus, W. Flood, M. Steigerwald, L. E. Brus, and M. G. Bawendi, *J. Phys. Chem.* **95**, 1572 (1991).
- <sup>59</sup>M. A. Marcus, L. E. Brus, C. Murray, M. G. Bawendi, A. Prasad, and A. P. Alivisatos, *Nanostruct. Mater.* **1**, 323 (1992).
- <sup>60</sup>J. Rockenberger, L. Tröger, A. Kornowski, T. Vossmeier, A. Eychmüller, J. Feldhaus, and H. Weller, *J. Phys. Chem. B* **101**, 2691 (1997).
- <sup>61</sup>J. Rockenberger, L. Tröger, A. L. Rogach, M. Tischer, M. Grundmann, A. Eychmüller, and H. Weller, *J. Chem. Phys.* **108**, 7807 (1998).
- <sup>62</sup>D. R. Pyke, R. Reid, and R. J. D. Tilley, *J. Solid State Chem.* **25**, 230 (1978).
- <sup>63</sup>S. Samson and C. G. Fonstadt, *J. Appl. Phys.* **44**, 4618 (1973).
- <sup>64</sup>C. Terrier, J. P. Chatelon, and J. A. Roger, *Thin Solid Films* **295**, 95 (1997).